

Structural basis of small-molecule inhibition of human multidrug transporter ABCG2

Scott M. Jackson^{1,6}, Ioannis Manolaridis^{1,6}, Julia Kowal^{1,6}, Melanie Zechner^{2,6}, Nicholas M. I. Taylor^{3,5,6}, Manuel Bause⁴, Stefanie Bauer⁴, Ruben Bartholomaeus², Guenther Bernhardt⁴, Burkhard Koenig⁴, Armin Buschauer^{4,7}, Henning Stahlberg³, Karl-Heinz Altmann^{2*} and Kaspar P. Locher^{1*}

ABCG2 is an ATP-binding cassette (ABC) transporter that protects tissues against xenobiotics, affects the pharmacokinetics of drugs and contributes to multidrug resistance. Although many inhibitors and modulators of ABCG2 have been developed, understanding their structure–activity relationship requires high-resolution structural insight. Here, we present cryo-EM structures of human ABCG2 bound to synthetic derivatives of the fumitremorgin C-related inhibitor Ko143 or the multidrug resistance modulator tariquidar. Both compounds are bound to the central, inward-facing cavity of ABCG2, blocking access for substrates and preventing conformational changes required for ATP hydrolysis. The high resolutions allowed for de novo building of the entire transporter and also revealed tightly bound phospholipids and cholesterol interacting with the lipid-exposed surface of the transmembrane domains (TMDs). Extensive chemical modifications of the Ko143 scaffold combined with in vitro functional analyses revealed the details of ABCG2 interactions with this compound family and provide a basis for the design of novel inhibitors and modulators.

ABCG2, also known as breast cancer resistance protein (BCRP), is a constitutively expressed ABC transporter with physiological roles in many tissues including the blood–brain and blood–testis barriers, the liver, the kidney and the mammary glands^{1–4}. Dysfunction of ABCG2 is linked to hyperuricemia, which can result in gout, kidney disease and hypertension, all of which are thought to be a consequence of the impaired transport of uric acid⁵. ABCG2, like its functional homologs ABCB1 (P-glycoprotein) and ABCC1 (MRP1), has a major protective role against xenobiotics. It affects the pharmacokinetics of many commonly used drugs, and its expression correlates with a poor prognosis and treatment outcome of certain cancers^{6–10}. ABCG2 has broad substrate specificity, with a certain preference for flat, polycyclic, hydrophobic compounds^{11–15}.

Because of their potential value as adjuvants in the treatment of cancer and pharmacotherapy, extensive efforts have been directed over the past decades to the development of specific inhibitors against human ABCG2 and other multidrug ABC transporters^{1,16–20}. The fungal toxin fumitremorgin C (FTC) is a selective inhibitor of ABCG2 but has undesirable neurotoxic effects^{16,21,22}. To reduce neurotoxicity, synthetic tetracyclic analogs of FTC have been developed. Among them, Ko143 was found to be more potent and less toxic than FTC, but it is not stable in mouse plasma and has been reported to have nonspecific effects on the transport activities of ABCB1 and ABCC1 at concentrations above 1 μM ²³. Attempts have also been made to develop selective ABCG2 inhibitors derived from tariquidar, a third-generation ABCB1 inhibitor reported to be a potential substrate of ABCG2 (refs ^{20,24–28}).

There is at present no structure of a human multidrug transporter bound to specific inhibitors. All of the above approaches aimed at developing specific inhibitors were made in the absence of structural insight into how the small compounds may interact with, modulate or inhibit ABCG2. Recently, the first structure of human ABCG2 revealed two cholesterol molecules bound at a central, inward-facing cavity, hinting at a potential location where substrates such as estrone-3-sulfate (E₃S) might bind²⁹. However, it remained unknown where inhibitors bind ABCG2 and whether a single or multiple ligand-binding sites exist, topics that are hotly debated^{30–34}. To address these questions, we determined single-particle cryo-EM structures of nanodisc-reconstituted human ABCG2 bound to distinct inhibitors. The high resolution obtained not only allowed the first de novo building of an atomic structure of the entire human ABCG2 protein, but also provided detailed insight into inhibition of the transporter by small molecules. By synthesizing a range of Ko143-derived compounds and testing their activity in vitro, we also obtained crucial information into the structure–activity relationship (SAR) of the Ko143 scaffold. Finally, we demonstrate that depending on the size of the compounds, one or two inhibitor molecules are required for full inhibition of ABCG2. These results provide an essential structural basis for future development of ABCG2 modulators.

Results

Synthesis of inhibitory compounds selective for ABCG2. Owing to its high selectivity for ABCG2, we used Ko143 as a starting point

¹Institute of Molecular Biology and Biophysics, Department of Biology, ETH Zurich, Zurich, Switzerland. ²Institute of Pharmaceutical Sciences, Department of Chemistry and Applied Biosciences, ETH Zurich, Zurich, Switzerland. ³Center for Cellular Imaging and NanoAnalytics (C-CINA), Biozentrum, University of Basel, Basel, Switzerland. ⁴Faculty of Chemistry and Pharmacy, University of Regensburg, Regensburg, Germany.

⁵Present address: Novo Nordisk Foundation Center for Protein Research, Faculty of Health and Medical Sciences, University of Copenhagen, Copenhagen, Denmark. ⁶These authors contributed equally: Scott M. Jackson, Ioannis Manolaridis, Julia Kowal, Melanie Zechner and Nicholas M. I. Taylor.

⁷Deceased: Armin Buschauer. *e-mail: karl-heinz.altmann@pharma.ethz.ch; locher@mol.biol.ethz.ch

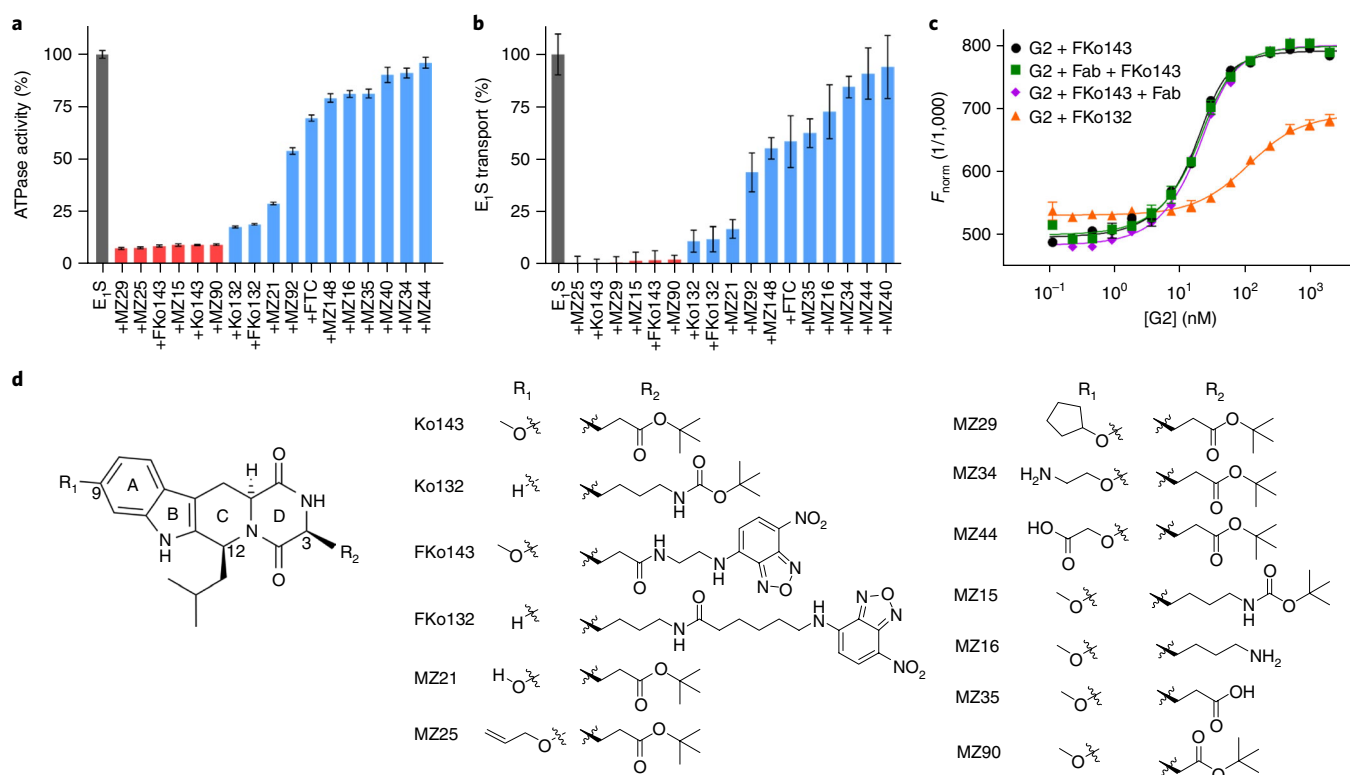


Fig. 1 | Functional characteristics of Ko143 derivatives. **a**, Normalized E₁S-stimulated ATPase activity of ABCG2 in proteoliposomes. **b**, Normalized initial E₁S transport rates in proteoliposomes. Assays in **a** and **b** were performed in the presence of 50 μM E₁S and in the absence or presence of 0.5 μM competitor. Bars representing compounds with potencies equal to or higher than that of Ko143 are in red, whereas those with lower potencies are in blue. Error bars indicate the s.d. of technical replicates, $n \geq 3$. **c**, MST binding assays used to determine dissociation constants (K_d) of FKo143 and FKo132 binding to ABCG2. ABCG2 was either incubated with FKo143 only (black curve, G2 + FKo143), preincubated with 5D3-Fab before the addition of FKo143 (green curve, G2 + Fab + FKo143), preincubated with FKo143 before the addition of 5D3-Fab (purple curve, G2 + FKo143 + Fab) or incubated with FKo132 only (orange curve, G2 + FKo132). Error bars indicate the s.d. of technical replicates, $n \geq 4$. **d**, Molecular structure of the Ko143 scaffold, with the C-3, C-9 and C-12 positions numbered and rings A–D labeled. Changes at the C-9 (R_1) and C-3 (R_2) positions are shown. Source data for **a–c** are available in Supplementary Dataset 1.

for the synthesis of novel compounds (Fig. 1, Supplementary Table 1 and Supplementary Notes). We mainly focused on modifications of the C-3 (R_2) and C-9 (R_1) positions of the Ko143 scaffold, because previous studies have demonstrated that the inhibitory capacities of FTC and its derivatives are affected by changes at these positions^{16,35}. Seventeen compounds were synthesized and screened in vitro for their ability to inhibit the E₁S-stimulated ATPase activity and initial E₁S transport activity of ABCG2 in proteoliposomes²⁹, and similar trends were observed in the ranking of their inhibitory capacities (Fig. 1a,b and Supplementary Table 2). We found that five compounds were as potent as Ko143 or slightly superior. Compound MZ29, which contained an O-cyclopentyl group added to the C-9 position, was found to be the most potent inhibitor of ATPase activity and fully abolished E₁S transport. In addition, similarly to Ko143 but unlike E₁S, MZ29 had a significant thermostabilizing effect on ABCG2 (Supplementary Fig. 1a,b and Supplementary Table 3), suggesting that it caused conformational stabilization, and was therefore selected for structural studies.

For high-resolution structure determination by cryo-EM, we added the conformational antigen-binding fragment of the human-specific 5D3 antibody (Fab) to inhibitor-bound ABCG2 (refs^{29,36}) (Figs. 2–4 and Supplementary Figs. 2–6). The addition of two Fabs increased the particle mass by ~100 kDa, which aided cryo-EM analysis, allowing for higher-resolution reconstruction. To rule out that the Fab altered the conformation of ABCG2 and diminished the mechanistic insight, we also determined the

structure of MZ29-bound ABCG2 in the absence of Fab, which was found to be indistinguishable from the Fab-bound structure (below and Supplementary Figs. 7 and 8). Furthermore, we investigated whether Fab would affect the binding of a synthetic, fluorescent Ko143 derivative (FKo143) to ABCG2. FKo143 contains a fluorescent NBD group at the C-3 position, which did not alter its inhibitory capacity (Fig. 1a,b,d), thus enabling us to measure its binding affinity by microscale thermophoresis (MST) (Fig. 1c and Supplementary Table 4). By determining dissociation constants, we found that the binding of FKo143 to ABCG2 was unaffected by Fab, providing strong support for the structural data and highlighting the functional relevance of the inhibitor-bound ABCG2–Fab structures.

Structures of the ABCG2–MZ29 complexes. The structure of nanodisc-reconstituted ABCG2 bound to MZ29 and two Fabs (ABCG2–MZ29–Fab) was determined at an overall resolution of 3.1 Å (Table 1, Fig. 2 and Supplementary Figs. 1–4). The TMDs and the ABCG2–Fab interface were well resolved (resolution around 2.5 Å), allowing the identification of two bound MZ29 molecules (Fig. 2a,b and Supplementary Figs. 3 and 4). The density for the nucleotide-binding domains (NBDs), which previously had only been modeled, owing to lower resolution²⁹, was also of excellent quality (Supplementary Fig. 4), allowing de novo building and thus providing the first complete atomic structure of human ABCG2. The conformation of the TMDs in the ABCG2–MZ29–Fab structure was found to be inward facing, similar to that of the previously

Table 1 | Cryo-EM data collection, refinement and validation statistics

	ABCG2-MZ29-Fab (EMD-3953, PDB 6ETI)	ABCG2-MB136-Fab (EMD-4246, PDB 6FEQ)	ABCG2-MZ29 (EMD-4256, PDB 6FFC)
Data collection and processing			
Magnification (nominal)	59,523 (165,000)	46,948 (130,000)	59,523 (165,000)
Voltage (kV)	300	300	300
Electron exposure (e ⁻ /Å ²)	2.0	1.6	2.0
Defocus range (μm)	-0.4 to -2.7	-0.4 to -2.5	-0.5 to -3.9
Pixel size (Å)	0.840	1.065	0.812
Symmetry imposed	C2	C1	C2
Initial particle images (no.)	587,743	529,097	2,098,186
Final particle images (no.)	284,831	306,913	402,348
Map resolution (Å)	3.10	3.60	3.56
FSC threshold	0.143	0.143	0.143
Map resolution range (Å)	3.0 to 9.0	3.0 to 9.0	3.0 to 9.0
Refinement			
Initial model used	PDB 5NJ3	PDB 6ETI	PDB 6ETI
Model resolution (Å)	3.10	3.60	3.56
FSC threshold	0.143	0.143	0.143
Model resolution range (Å)	322.5-3.1	322.5-3.1	259.7-3.6
Map-sharpening B factor (Å ²)	-98	-163	-171
Model composition			
Nonhydrogen atoms	12,366	-	8,898
Protein residues	1,582	-	1,144
Ligands	76	-	76
B factors (Å²)			
Protein	52.42	-	44.69
Ligand	49.94	-	12.47
R.m.s. deviations			
Bond lengths (Å)	0.01	-	0.007
Bond angles (°)	1.02	-	0.93
Validation			
MolProbity score	1.47	-	1.44
Clashscore	3.06	-	3.66
Poor rotamers (%)	0.30	-	0.00
Ramachandran plot			
Favored (%)	94.48	-	95.92
Allowed (%)	5.33	-	3.90
Disallowed (%)	0.19	-	0.18

The refinement statistics for the final model of ABCG2-MZ29-Fab include only the variable domains of Fab.

determined ABCG2-cholesterol-Fab structure, with a slit-like cavity (cavity 1) accessible both from the cytoplasmic side of the membrane and from the inner leaflet of the lipid bilayer. Cavity 1 is separated from a second cavity (cavity 2) by a 'leucine plug' formed by L554 of opposing monomers (Fig. 2c,d) and was previously shown to be optimally suited to bind relatively flat, hydrophobic, polycyclic molecules²⁹, a feature that is distinct from the multidrug transporters ABCB1 and ABCC1, which form more globular cavities^{37,38}. Access to cavity 1 from the lipid bilayer occurs via a hydrophobic 'membrane entrance' lined by residues A397, V401, L405, L539, I543 and F547 from transmembrane (TM) helices TM1b and TM5a of opposing monomers (Fig. 2e,f). The EM density clearly revealed two MZ29 molecules bound in cavity 1, each between TM1b and TM2 of one ABCG2 monomer and TM5a of the other.

The binding pockets are close to the two-fold symmetry axis of ABCG2, and the two MZ29 molecules occupy almost the entire volume of cavity 1, thereby preventing the binding of other molecules, such as transport substrates (Fig. 2b-d). Cavity 2, which is fully occluded between the leucine plug and the extracellular loops, does not contain any density features, indicating that no ordered inhibitors or substrates are bound at this site.

At the bottom of cavity 1 (furthest from the cytoplasmic membrane boundary), the hydrophobic residues F431, F432, M549 and L555 interact with the O-cyclopentyl group of MZ29 (Fig. 2e). In addition, the O-cyclopentyl groups of the two MZ29 molecules are 3.7 Å apart, probably forming van der Waals interactions with one another. T435 forms a hydrogen bond with the oxygen at the C-9 position, and a series of polar and hydrophobic residues,

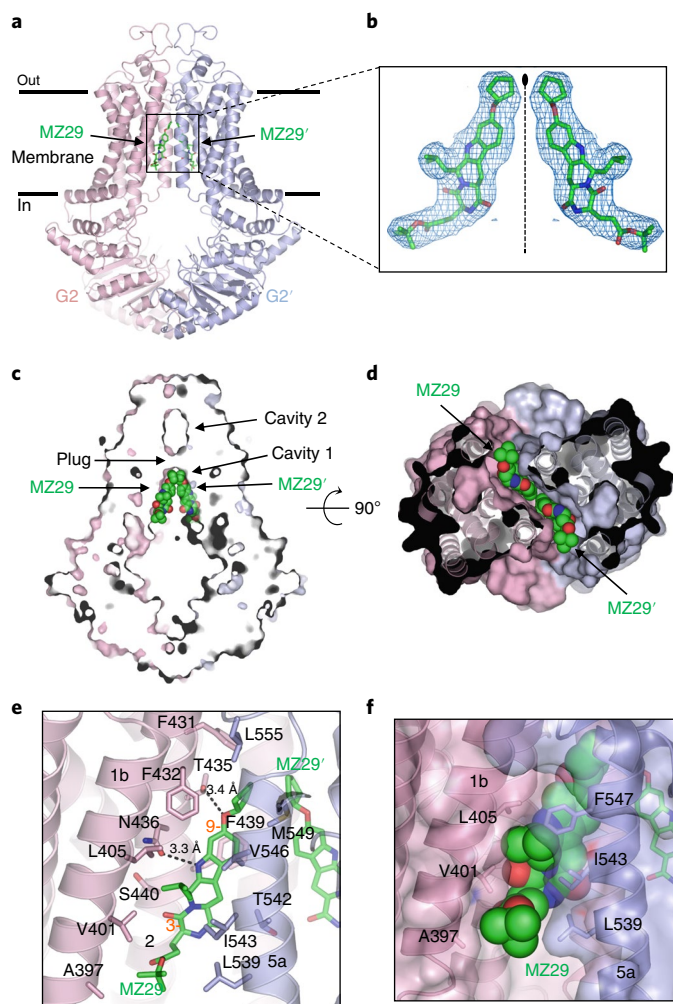


Fig. 2 | Structure of the ABCG2-MZ29-Fab complex. **a**, Ribbon diagram of the ABCG2 homodimer, with individual G2 monomers colored pink and purple. The two Fabs were removed for clarity. Bound MZ29 molecules are shown as green sticks and are labeled. **b**, EM density with bound MZ29 molecules, with the view rotated by 45° relative to that in **a**. The dotted line represents the two-fold symmetry axis. **c**, Vertical slice through a surface representation of ABCG2 with bound MZ29 shown as green spheres and labeled. Cavities 1 and 2 and the leucine plug are indicated. **d**, Cavity 1 viewed from the cytoplasm, with NBDs of ABCG2 removed for clarity and bound MZ29 shown as green spheres and labeled. **e**, Specific interactions between MZ29 and ABCG2 residues in cavity 1. Interacting residues are shown as sticks and labeled, and hydrogen bonds are shown as dashed lines. The C-3 and C-9 positions of MZ29 are labeled in orange. TM helices are labeled 1b, 2, and 5a. **f**, Transparent surface representation of the hydrophobic membrane entrance region of ABCG2 viewed from within the membrane, with one MZ29 molecule shown as green spheres and contacting ABCG2 residues shown as sticks and labeled.

including S440, T542 and V546, form van der Waals interactions with the polycyclic core of MZ29. Furthermore, N436 forms a hydrogen bond with the NH group of the indole ring, and F439 forms a stacking interaction with the benzene ring of the indole moiety. Residues V401, L405, I543, V546 and F547 form van der Waals interactions with the isobutyl group at the C-12 position, whereas A397, V401, L539 and I543 interact with the *tert*-butyloxy-carbonyl group at the C-3 position.

Our functional analyses of synthetic Ko143 derivatives allowed us to probe the specific interactions between cavity 1 and the inhibitor in the context of wild-type ABCG2 (Supplementary Table 5).

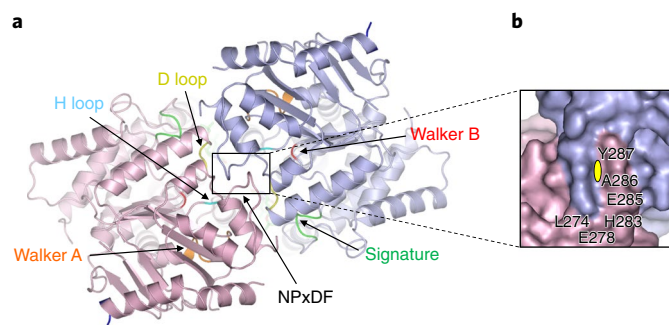


Fig. 3 | ABCG2 NBDs. **a**, The ABCG2 NBDs with the D loop, H loop, Walker A, Walker B, signature and NPxDF motifs labeled. **b**, Surface representation of ABCG2 showing the contact point at the bottom of the two NBDs with residues indicated and a yellow ellipsoid marking the two-fold symmetry axis.

The inhibitory capacity of the Ko143 derivatives was more affected by changes at the C-9 position than at the C-3 position (Fig. 1a,b,d). Removal of the methoxy group at the C-9 position caused a ~22-fold reduction in binding affinity, as shown by differences in the dissociation constants measured for FK0143 versus FK0132 (Fig. 1c and Supplementary Table 4). This reduction in affinity and in inhibitory potency (Ko143, FK0143 and MZ15 versus Ko132 and FK0132, Fig. 1a,b) confirmed the importance of the hydrogen bond between the methoxy group of Ko143 and T435 in cavity 1 (refs 16,21,22,35) (Fig. 2e). Whereas small hydrophobic additions to the C-9 position (as in MZ25 and MZ29) did not affect potency, the addition of hydrophilic groups (MZ34, MZ44) led to inactive compounds, probably because of chemical mismatch with the hydrophobic ABCG2 surface at the bottom of the cavity. Removal of the methyl group at the C-9 position (MZ21) also caused a drop in potency, which could be due to the hydrophilicity of the resulting hydroxyl group or the absence of hydrophobic interactions with residues at the bottom of cavity 1. The exchange of the *tert*-butyloxy-carbonyl end group of the substituent at the C-3 position with either a positively (as in MZ16) or a negatively charged (as in MZ35) moiety resulted in a substantial decrease in inhibitory capacity, probably due to the mismatch with the hydrophobic side chains in the vicinity of the membrane entrance (Fig. 2f). Likewise, the expansion of the diketopiperazine ring by one carbon atom (MZ92, Supplementary Table 1) caused a marked reduction of potency, possibly because the *tert*-butyloxy-carbonyl group of the side chain was shifted, reducing the number of van der Waals interactions. Intriguingly, the inversion of the C-12 position from the *R* to the *S* configuration completely eliminated the inhibitory capability of the resulting diastereoisomer (MZ40, Supplementary Table 1), most likely because of an ensuing steric clash with residue N436. Finally, we can rationalize why FTC is less potent than Ko143: the E ring of FTC, as well as MZ148, cannot form favorable interactions with residues at the membrane entrance, which reduces the inhibitory potencies of these compounds.

We also determined the cryo-EM structure of nanodisc-reconstituted ABCG2 in complex with MZ29, but in the absence of Fab, (ABCG2-MZ29) at an overall resolution of 3.6 Å (Table 1 and Supplementary Figs. 7 and 8). With the exception of the external loop EL3, which is in direct contact with Fab, the structure was indistinguishable from that of the Fab-bound form, and no differences in side chain conformations were detected at this resolution (Supplementary Fig. 8f). Two MZ29 molecules were bound at exactly the same positions and in the same orientations as in the Fab-bound structure. However, the resolution was lower despite a much larger number of particles used in the 3D reconstruction, demonstrating that the use of 5D3-Fab facilitated structure determination at significantly higher resolution (Table 1 and

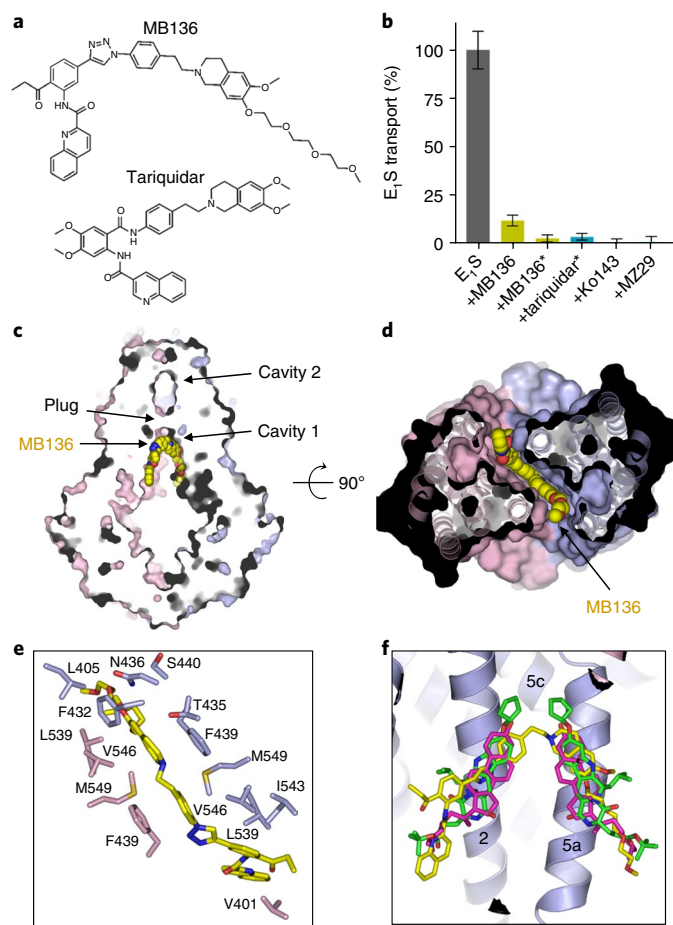


Fig. 4 | Structure of MB136-bound ABCG2 revealing a central multidrug-binding site. **a**, Molecular structures of MB136 and tariquidar. **b**, Normalized initial E_1S transport rates of proteoliposome-reconstituted ABCG2 in the presence of 50 μM E_1S and the absence or presence of 0.5 μM competitor, except for '+MB136*' and '+tariquidar*' for which the concentration was 10 μM . Error bars represent the s.d. of technical replicates, $n \geq 3$. **c**, Vertical slice through a surface representation of ABCG2, with bound MB136 shown as yellow spheres and labeled. Cavities 1 and 2 and the leucine plug are indicated. **d**, Cavity 1 viewed from the cytoplasm, with NBDs of ABCG2 removed for clarity and bound MB136 shown as yellow spheres and labeled. **e**, Extracellular view of cavity 1 showing the side chains of residues, displayed as sticks, within 4 Å of MB136 (yellow sticks). **f**, Overlay of the bound ligands in cavity 1 from the structures of ABCG2 with bound cholesterol (purple sticks, PDB 5NJ3), MZ29 (green sticks) and MB136 (yellow sticks) after superposition of the ABCG2 TMDs from the three structures. Source data for **b** are available in Supplementary Dataset 1.

Supplementary Figs. 2 and 7), which is paramount for the detailed study of protein–ligand interactions.

Structure of the ABCG2–MB136–Fab complex. We sought to explore whether a different class of inhibitor could bind in the same pocket (cavity 1) as MZ29 or cholesterol. We synthesized and evaluated derivatives of tariquidar²⁸, a compound developed as a specific inhibitor of ABCB1, but whose phase III trials were discontinued mainly because of chemotherapy-related toxicity³⁹. During systematic modification of tariquidar (Fig. 4a and Supplementary Notes), it was observed that selectivity was drastically shifted from ABCB1 to ABCG2 by small alterations of the substitution pattern at the aromatic core⁴⁰. To improve metabolic

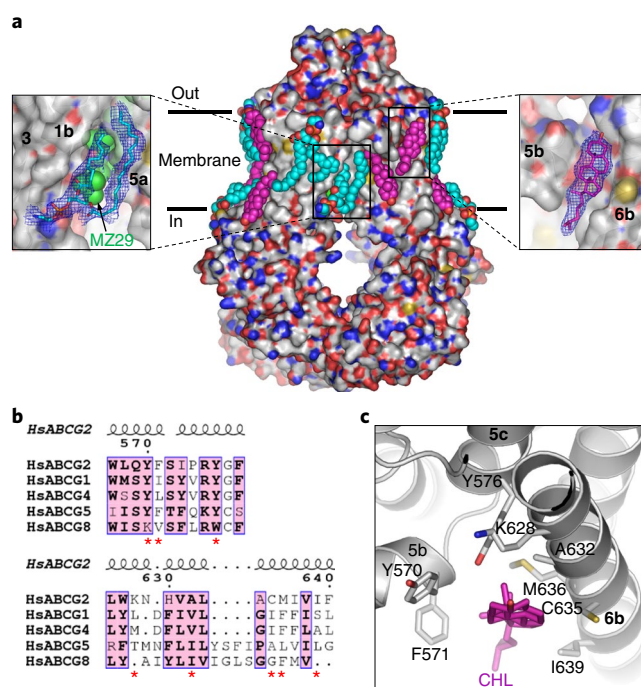


Fig. 5 | ABCG2–lipid interactions. **a**, Surface representation of ABCG2 colored according to atom type. Bound cholesterol molecules are shown as pink spheres, phospholipids are shown as cyan spheres, and bound MZ29 are shown as green spheres. Inserts, EM density with a bound cholesterol molecule indicated as pink sticks (right) and a bound phospholipid molecule, localized at the membrane entrance, indicated as cyan sticks (left). The numbers shown in the inserts refer to TM helices. **b**, Alignment of the G-subfamily ABC transporters showing residue conservation in the ABCG2 cholesterol 'groove'. Red asterisks highlight the residues shown in **c**. **c**, The best-resolved cholesterol groove as viewed from the extracellular side. Residues interacting with the bound cholesterol are shown as sticks.

stability, the labile amide moiety was replaced with a triazole ring, and 'pegylation' was used to improve water solubility^{24,26}. The resulting compound, MB136, is a novel fourth-generation modulator of ABCG2, containing a triazole core and a propionyl side chain on the phenyl ring (Fig. 4a). MB136 and tariquidar inhibited E_1S transport by proteoliposome-reconstituted ABCG2, but both were less potent than Ko143 and MZ29 (Fig. 4b and Supplementary Table 2). Indeed, only at higher concentrations of MB136 and tariquidar was E_1S transport fully abolished. MB136 thermostabilized ABCG2 to a similar extent as Ko143 or MZ29 (Supplementary Fig. 1b and Supplementary Table 3).

We determined the cryo-EM structure of nanodisc-reconstituted ABCG2 in complex with MB136 and Fab (ABCG2–MB136–Fab) at an overall resolution of 3.6 Å, with the best-resolved regions around 3.0 Å (Table 1, Fig. 4c–e and Supplementary Figs. 5 and 6). The EM map revealed a strong density feature in cavity 1, overlapping in location to where MZ29 or cholesterol were previously observed (Fig. 4f). This density was distinct in shape from that observed for MZ29 and could only fit one MB136 molecule. The initial processing of the data with C2 symmetry resulted in an averaged density for MB136 that was very broad, especially close to the two-fold symmetry axis (Supplementary Fig. 6e). When the data were reprocessed with C1 symmetry, asymmetric features appeared in the density that allowed us to place MB136 and pinpoint specific interactions (Supplementary Fig. 6f). The fact that the fit of the EM density was not as high for MB136 as that of MZ29 suggested that MB136, despite its inhibitory capability (Fig. 4b), may have multiple modes of binding by moving or sliding within cavity 1.

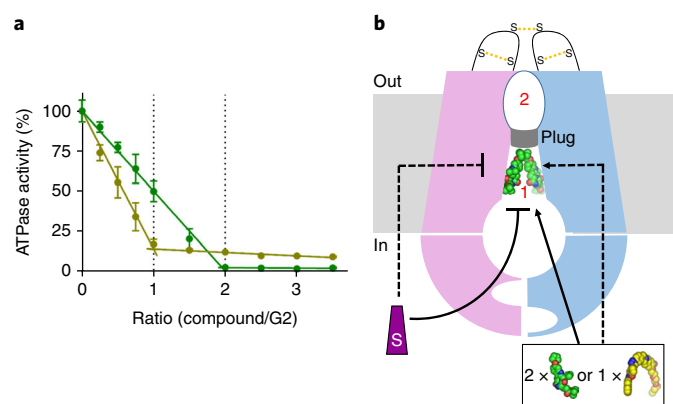


Fig. 6 | Proposed mechanism of inhibition. **a**, Normalized ATPase activity of nanodisc-reconstituted ABCG2 at varying inhibitor to ABCG2 (homodimer) ratios with Ko143 in green and MB136 in yellow. The mean from two independent protein preparations is plotted and error bars represent the s.d. ($n \geq 4$). **b**, Schematic of ABCG2 inhibition by small molecules. ABCG2 monomers are colored pink and blue, disulfide bridges at EL3 are indicated by yellow dashed lines connecting sulfur atoms, the red numbers (1 and 2) indicate cavities 1 and 2, and the leucine plug is shown as a gray bar between the cavities. The binding of two MZ29 molecules (green spheres) or one MB136 molecule (yellow spheres) blocks cavity 1 and locks ABCG2 in an inward-facing open conformation. This binding may prevent substrate (purple trapezoid) access to cavity 1 and, simultaneously, the NBDs from closing and hydrolyzing ATP. Source data for **a** are available in Supplementary Dataset 1.

Cholesterol and phospholipids bound to the TMDs. The high resolution of the EM maps and the presence of a physiologically relevant mix of lipids in the nanodisc (brain polar lipid extract) allowed us to visualize and characterize ABCG2–lipid interactions. While ordered lipids were observed at similar locations in all three structures, we used the highest resolution structure (ABCG2–MZ29–Fab) for the building of the lipid molecules. Ordered membrane cholesterol and phospholipids form a belt around ABCG2, thus marking the boundary of the lipid bilayer and matching the hydrophobic protein surface (Fig. 5a). It was previously demonstrated that membrane cholesterol has an essential role for ABCG2 function, and it has been proposed that ABCG2 is mainly localized in lipid rafts of the plasma membrane, where the cholesterol concentration is high^{41,42}. Thus, the ordered cholesterol molecules visualized in our structure are likely to be of functional importance. We identified five ordered cholesterol molecules per ABCG2 monomer, tightly bound in hydrophobic grooves. The best-ordered cholesterol is located between TM5b, TM5c and TM6b and interacts with a number of hydrophobic residues (Fig. 5). Although the TMD architectures of G-subfamily ABC transporters are probably similar, this specific pocket for cholesterol on the ABCG2 surface appears unique because the interacting residues are not conserved (Fig. 5b) and because no cholesterol-binding groove was observed in the crystal structure of the human liver cholesterol transporter ABCG5/ABCG8 (hereafter abbreviated as G5G8)⁴³. Although studies have suggested that residues L555–L558 of ABCG2 contribute to sterol binding or sensing⁴⁴, it has been shown that the relevant motif was in fact not important for cholesterol binding by ABCG2 (ref. 45). Our structure reveals that residues L555–L558 are not facing the lipid bilayer but are located in the core of ABCG2 and are some 12 Å away from the closest ordered cholesterol molecule. Therefore, these residues cannot bind membrane cholesterol directly, and the reported effects are likely to be allosteric in nature. We were also able to dock five annular phospholipids per ABCG2 monomer, which we modeled as phosphatidylethanolamine (PE), owing to its abundance in the lipid extract used for nanodisc generation. Intriguingly, one of

the phospholipids covers the membrane entrance of ABCG2 and must therefore move if a substrate or inhibitor requires access to cavity 1 from within the lipid bilayer (Fig. 5a).

Insight into the nucleotide-binding domains. The high resolution and conformational homogeneity of the inhibitor-bound ABCG2 structures allowed for a de novo build of the NBDs, with clear side chain density (Fig. 3 and Supplementary Fig. 4). In the absence of nucleotides, the NBDs are in a functionally ‘open’ conformation (apo state), with a gap between the catalytically relevant motifs. Nevertheless, the NBDs remain in contact, with approximately 680 Å² of buried surface. The contact point is formed mainly by residues preceding the NPxDF motif (289–NPADF–293 for ABCG2), which is conserved in all G-subfamily ABC transporters⁴⁴ (Fig. 3). The overall fold of the NBDs is similar to that of G5G8, with an overall r.m.s. deviation (r.m.s.d.) of 2.3 Å and a sequence identity of 33% (ref. 43). The distance between the Walker A and ABC signature motifs is 16.9 Å in ABCG2 compared to the 16.5 Å for G5G8, suggesting a shared NBD spacing for all G-subfamily ABC transporters in the nucleotide-free state. The linker connecting the last α -helix of the NBDs, containing the C2 motif⁴⁶, with TM1a is not visible in our maps, nor was it observed in the structure of G5G8, most likely because of its inherent flexibility.

The mutation Q141K is a reported single-nucleotide polymorphism (SNP) of ABCG2 associated with hyperuricemia and gout. It results in decreased expression or degradation of the protein, probably due to misfolding^{47,48}. Our structure shows that Q141 is located in the NBD on an α -helix adjacent to TM1a of the TMD, where it can form a hydrogen bond with N158, confirming the previous in silico predictions^{31,34} (Supplementary Fig. 4e). Given that this is a critical, non-covalent interaction between the NBD and TMD, our structures can rationalize the detrimental effect of this mutation on protein folding and function. Finally, it has also been suggested that C284, C374 and C438 form intramolecular disulfide bonds that are important for ABCG2 function⁴⁹. Our structures reveal that these cysteines are distantly located, and their functional roles are therefore unrelated to disulfide bond formation.

Stoichiometry of small-molecule inhibition. To validate our structural findings of two Ko143 derivatives (MZ29), but only one MB136 molecule bound to ABCG2, we investigated how many inhibitor molecules were required to impair the ATPase activity of ABCG2 in nanodiscs (Supplementary Table 2). We found that maximal inhibition was obtained at a ratio of one MB136 molecule for each ABCG2 homodimer. In contrast, two molecules of Ko143 were required for full inhibition (Fig. 6a). These results are in full agreement with our structural data that reveal the same stoichiometries. We observed an ~50% inhibition of ATPase activity when the molar ratio of Ko143 to ABCG2 homodimer was 1:1. This finding can be interpreted in two ways: a single Ko143 may be bound to every ABCG2 homodimer, reducing its activity by 50%; alternatively, half of the ABCG2 homodimers may contain two bound Ko143 molecules and are completely inhibited, whereas the other half contain no inhibitor and are active. While the high affinity of MZ29 did not allow a direct observation, we propose that the latter explanation is more likely because positive cooperativity can be invoked.

Discussion

Our results represent the first structures of a human multidrug transporter bound to specific, small-molecule inhibitors. Both MZ29 and MB136 bind in the same cavity as the previously observed cholesterol molecules²⁹. Cholesterol bound to cavity 1 either represents an analog of the bona fide substrate E,S in ABCG2 or is a known substrate in other G-subfamily ABC transporters. We therefore conclude that cavity 1 in ABCG2 represents a multidrug-binding site, although future substrate-bound structures

are needed to validate the hypothesis that all substrates bind in this pocket. ABCG2 exhibits conformational rigidity within cavity 1, irrespective of the ligand bound, and we hypothesize that this reduces the spectrum of ligands that can bind to ABCG2. Nevertheless, binding of distinct molecules has drastically different consequences: when cholesterol was bound to cavity 1, the ATPase rate was fully stimulated²⁹, whereas it was abolished when MZ29 or MB136 was bound. This finding demonstrates that even though the conformation of ABCG2 may be similar (inward open), and the shape of cavity 1 is conserved, the transporter readily distinguishes between substrates and inhibitors in the presence of ATP. Although cavity 1 can bind one or two inhibitors symmetrically or asymmetrically, depending on their size and shape, it remains to be demonstrated whether the same holds for substrates in a productive transport cycle, i.e., whether two substrates may be transported during a single cycle.

Recently, in silico models of human ABCG2 were reported^{31,34} that used the G5G8 crystal structure⁴³ as a modeling template. The G5G8 structure is different from that of ABCG2 in that it does not form a central, inward-facing cavity, a feature critical to the binding of small compounds in ABCG2, as revealed in this study. Based on the in silico model, mutagenesis experiments were conducted, and some of the mutants showed changes in ABCG2 function in a cellular context³⁴. However, none of the tested side chains are located in cavity 1 or interact with the inhibitory compounds in our structures. The observed functional effects might therefore be due to allosteric interactions or possibly direct contacts with substrates when ABCG2 adopts a different conformation from the inward-facing state reported here.

It is widely accepted that binding affinity is a key determinant of whether a molecule will be a transported substrate or an inhibitor without 'measurable' transport. Indeed, many substrates for ABCG2 have affinities in the low micromolar range^{29,50,51}, whereas potent inhibitors, such as Ko143, have low nanomolar dissociation constants or IC₅₀ values^{24–26}. We observed an ~3,000-fold difference in affinity between E_S²⁹ and FKo143 (Fig. 1c and Supplementary Table 4). We speculate that substrates would bind in cavity 1 before moving toward cavity 2 in order to be transported, whereas inhibitors would remain tightly bound in cavity 1 without detectable transport. Because of the conformational coupling of the TMDs and NBDs, the movement of substrate is a prerequisite for the closing of cavity 1, the conversion of the TMDs to an inward-closed conformation and the concomitant closure of the NBD dimer. In a productive transport cycle, NBD-dimer closure is expected to result in the conversion of ABCG2 from an inward- to an outward-facing conformation, followed by hydrolysis of ATP and the release of substrate to the outside (alternating-access mechanism). The effect of inhibitors binding to cavity 1 would be twofold. First, given their higher affinities, the binding of substrates is prevented by the inhibitors as they almost completely occupy the volume provided by cavity 1. In this sense, the inhibitors presented here act competitively. Whereas less potent inhibitors, such as MB136, may move or slide within the cavity, the more potent inhibitor MZ29 showed no signs of any motion within cavity 1. Second, both MZ29 and MB136 appear to lock the inward-facing state of the TMDs, which prevents closure of the NBDs due to conformational coupling, as evidenced by the inhibition of ATPase activity upon inhibitor binding (Figs. 1a and 6). Such tight conformational coupling might be due to the compact shape of ABCG2, which does not provide the same flexibility as the more elongated architectures of ABC transporters of the B and C subfamilies.

The inhibitor-bound structures of ABCG2 presented here should prove useful for guiding future functional experiments. They also

provide a long-sought basis for rational, structure-based inhibitor development against ABCG2. To understand the specific requirements of transported substrates, novel structures of substrate-bound states in distinct conformations are required.

Methods

Methods, including statements of data availability and any associated accession codes and references, are available at <https://doi.org/10.1038/s41594-018-0049-1>.

Received: 18 October 2017; Accepted: 12 February 2018;
Published online: 2 April 2018

References

- Crowley, E., McDevitt, C. A. & Callaghan, R. Generating inhibitors of P-glycoprotein: where to, now? *Methods Mol. Biol.* **596**, 405–432 (2010).
- Diestra, J. E. et al. Frequent expression of the multi-drug resistance-associated protein BCRP/MXR/ABCP/ABCG2 in human tumours detected by the BXP-21 monoclonal antibody in paraffin-embedded material. *J. Pathol.* **198**, 213–219 (2002).
- Fetsch, P. A. et al. Localization of the ABCG2 mitoxantrone resistance-associated protein in normal tissues. *Cancer Lett.* **235**, 84–92 (2006).
- Robey, R. W. et al. ABCG2: a perspective. *Adv. Drug Deliv. Rev.* **61**, 3–13 (2009).
- Ishikawa, T., Aw, W. & Kaneko, K. Metabolic interactions of purine derivatives with human ABC transporter ABCG2: genetic testing to assess gout risk. *Pharmaceuticals (Basel)* **6**, 1347–1360 (2013).
- Gillet, J. P. & Gottesman, M. M. Advances in the molecular detection of ABC transporters involved in multidrug resistance in cancer. *Curr. Pharm. Biotechnol.* **12**, 686–692 (2011).
- Gottesman, M. M., Fojo, T. & Bates, S. E. Multidrug resistance in cancer: role of ATP-dependent transporters. *Nat. Rev. Cancer* **2**, 48–58 (2002).
- Iorio, A. L. et al. Blood-brain barrier and breast cancer resistance protein: a limit to the therapy of CNS tumors and neurodegenerative diseases. *Anticancer. Agents Med. Chem.* **16**, 810–815 (2016).
- Sarkadi, B., Homolya, L., Szakács, G. & Váradi, A. Human multidrug resistance ABCB and ABCG transporters: participation in a chemoimmunity defense system. *Physiol. Rev.* **86**, 1179–1236 (2006).
- Sharom, F. J. The P-glycoprotein multidrug transporter. *Essays Biochem.* **50**, 161–178 (2011).
- Bakhsheshian, J. et al. Overlapping substrate and inhibitor specificity of human and murine ABCG2. *Drug Metab. Dispos.* **41**, 1805–1812 (2013).
- Imai, Y. et al. Breast cancer resistance protein exports sulfated estrogens but not free estrogens. *Mol. Pharmacol.* **64**, 610–618 (2003).
- Mao, Q. & Unadkat, J. D. Role of the breast cancer resistance protein (BCRP/ABCG2) in drug transport—an update. *AAPS J.* **17**, 65–82 (2015).
- Mo, W. & Zhang, J. T. Human ABCG2: structure, function, and its role in multidrug resistance. *Int. J. Biochem. Mol. Biol.* **3**, 1–27 (2012).
- Vlaming, M. L., Lagas, J. S. & Schinkel, A. H. Physiological and pharmacological roles of ABCG2 (BCRP): recent findings in Abcg2 knockout mice. *Adv. Drug Deliv. Rev.* **61**, 14–25 (2009).
- Allen, J. D. et al. Potent and specific inhibition of the breast cancer resistance protein multidrug transporter in vitro and in mouse intestine by a novel analogue of fumitremorgin C. *Mol. Cancer Ther.* **1**, 417–425 (2002).
- Holland, M. L., Lau, D. T., Allen, J. D. & Arnold, J. C. The multidrug transporter ABCG2 (BCRP) is inhibited by plant-derived cannabinoids. *Br. J. Pharmacol.* **152**, 815–824 (2007).
- Kannan, P. et al. The “specific” P-glycoprotein inhibitor Tariquidar is also a substrate and an inhibitor for breast cancer resistance protein (BCRP/ABCG2). *ACS Chem. Neurosci.* **2**, 82–89 (2011).
- Peterson, B. G., Tan, K. W., Osa-Andrews, B. & Iram, S. H. High-content screening of clinically tested anticancer drugs identifies novel inhibitors of human MRP1 (ABCC1). *Pharmacol. Res.* **119**, 313–326 (2017).
- Puentes, C. O. et al. Solid phase synthesis of tariquidar-related modulators of ABC transporters preferring breast cancer resistance protein (ABCG2). *Bioorg. Med. Chem. Lett.* **21**, 3654–3657 (2011).
- Rabindran, S. K. et al. Reversal of a novel multidrug resistance mechanism in human colon carcinoma cells by fumitremorgin C. *Cancer Res.* **58**, 5850–5858 (1998).
- Rabindran, S. K., Ross, D. D., Doyle, L. A., Yang, W. & Greenberger, L. M. Fumitremorgin C reverses multidrug resistance in cells transfected with the breast cancer resistance protein. *Cancer Res.* **60**, 47–50 (2000).
- Weidner, L. D. et al. The inhibitor Ko143 is not specific for ABCG2. *J. Pharmacol. Exp. Ther.* **354**, 384–393 (2015).

24. Bauer, S. et al. Quinoline carboxamide-type ABCG2 modulators: indole and quinoline moieties as anilide replacements. *ChemMedChem* **8**, 1773–1778 (2013).
25. Köhler, S. C. & Wiese, M. HM30181 derivatives as novel potent and selective inhibitors of the breast cancer resistance protein (BCRP/ABCG2). *J. Med. Chem.* **58**, 3910–3921 (2015).
26. Ochoa-Puentes, C. et al. Benzanilide-biphenyl replacement: a bioisosteric approach to quinoline carboxamide-type ABCG2 modulators. *ACS Med. Chem. Lett.* **4**, 393–396 (2013).
27. Pick, A., Klinkhammer, W. & Wiese, M. Specific inhibitors of the breast cancer resistance protein (BCRP). *ChemMedChem* **5**, 1498–1505 (2010).
28. Roe, M. et al. Reversal of P-glycoprotein mediated multidrug resistance by novel anthranilamide derivatives. *Bioorg. Med. Chem. Lett.* **9**, 595–600 (1999).
29. Taylor, N. M. I. et al. Structure of the human multidrug transporter ABCG2. *Nature* **546**, 504–509 (2017).
30. Haider, A. J. et al. Identification of residues in ABCG2 affecting protein trafficking and drug transport, using co-evolutionary analysis of ABCG sequences. *Biosci. Rep.* **35**, e00241 (2015).
31. László, L., Sarkadi, B. & Hegedűs, T. Jump into a new fold-A homology based model for the ABCG2/BCRP multidrug transporter. *PLoS One* **11**, e0164426 (2016).
32. Ni, Z., Bikadi, Z., Cai, X., Rosenberg, M. F. & Mao, Q. Transmembrane helices 1 and 6 of the human breast cancer resistance protein (BCRP/ABCG2): identification of polar residues important for drug transport. *Am. J. Physiol. Cell Physiol.* **299**, C1100–C1109 (2010).
33. Ni, Z. et al. Identification of proline residues in or near the transmembrane helices of the human breast cancer resistance protein (BCRP/ABCG2) that are important for transport activity and substrate specificity. *Biochemistry* **50**, 8057–8066 (2011).
34. Khunweeraphong, N., Stockner, T. & Kuchler, K. The structure of the human ABC transporter ABCG2 reveals a novel mechanism for drug extrusion. *Sci. Rep.* **7**, 13767 (2017).
35. van Loevezijn, A., Allen, J. D., Schinkel, A. H. & Koomen, G. J. Inhibition of BCRP-mediated drug efflux by fumitremorgin-type indolyl diketopiperazines. *Bioorg. Med. Chem. Lett.* **11**, 29–32 (2001).
36. Zhou, S. et al. The ABC transporter Bcrp1/ABCG2 is expressed in a wide variety of stem cells and is a molecular determinant of the side-population phenotype. *Nat. Med.* **7**, 1028–1034 (2001).
37. Aller, S. G. et al. Structure of P-glycoprotein reveals a molecular basis for poly-specific drug binding. *Science* **323**, 1718–1722 (2009).
38. Johnson, Z. L. & Chen, J. Structural basis of substrate recognition by the multidrug resistance protein MRP1. *Cell* **168**, 1075–1085.e9 (2017).
39. Gergely, S. et al. in *Drug Resistance in Cancer Cells* (eds Siddik, Z. & Mehta, K.) 1–20 (Springer, New York, 2009).
40. Kühnle, M. et al. Potent and selective inhibitors of breast cancer resistance protein (ABCG2) derived from the p-glycoprotein (ABC1) modulator tariquidar. *J. Med. Chem.* **52**, 1190–1197 (2009).
41. Storch, C. H., Ehehalt, R., Haefeli, W. E. & Weiss, J. Localization of the human breast cancer resistance protein (BCRP/ABCG2) in lipid rafts/caveolae and modulation of its activity by cholesterol in vitro. *J. Pharmacol. Exp. Ther.* **323**, 257–264 (2007).
42. Szilagyi, J. T., Vetrano, A. M., Laskin, J. D. & Aleksunes, L. M. Localization of the placental BCRP/ABCG2 transporter to lipid rafts: Role for cholesterol in mediating efflux activity. *Placenta* **55**, 29–36 (2017).
43. Lee, J. Y. et al. Crystal structure of the human sterol transporter ABCG5/ABCG8. *Nature* **533**, 561–564 (2016).
44. Telbisz, Á., Hegedűs, C., Váradi, A., Sarkadi, B. & Özvegy-Laczkó, C. Regulation of the function of the human ABCG2 multidrug transporter by cholesterol and bile acids: effects of mutations in potential substrate and steroid binding sites. *Drug Metab. Dispos.* **42**, 575–585 (2014).
45. Velamakanni, S., Janvilisri, T., Shahi, S. & van Veen, H. W. A functional steroid-binding element in an ATP-binding cassette multidrug transporter. *Mol. Pharmacol.* **73**, 12–17 (2008).
46. Macalou, S. et al. The linker region of breast cancer resistance protein ABCG2 is critical for coupling of ATP-dependent drug transport. *Cell. Mol. Life Sci.* **73**, 1927–1937 (2016).
47. Basseville, A. & Bates, S. E. Gout, genetics and ABC transporters. *F1000 Biol. Rep.* **3**, 23 (2011).
48. Furukawa, T. et al. Major SNP (Q141K) variant of human ABC transporter ABCG2 undergoes lysosomal and proteasomal degradations. *Pharm. Res.* **26**, 469–479 (2009).
49. Liu, Y., Yang, Y., Qi, J., Peng, H. & Zhang, J. T. Effect of cysteine mutagenesis on the function and disulfide bond formation of human ABCG2. *J. Pharmacol. Exp. Ther.* **326**, 33–40 (2008).
50. Ni, Z., Bikadi, Z., Rosenberg, M. F. & Mao, Q. Structure and function of the human breast cancer resistance protein (BCRP/ABCG2). *Curr. Drug Metab.* **11**, 603–617 (2010).
51. Suzuki, M., Suzuki, H., Sugimoto, Y. & Sugiyama, Y. ABCG2 transports sulfated conjugates of steroids and xenobiotics. *J. Biol. Chem.* **278**, 22644–22649 (2003).

Acknowledgements

This research was supported by the Swiss National Science Foundation through the National Centre of Competence in Research (NCCR) TransCure and by a Swiss Federal Institute of Technology Zurich (ETH Zurich) research grant ETH-22-14-1. J.K. was also supported by the TransCure Young Investigator Award. N.M.I.T. was also supported by the University of Basel Research Fund for Junior Investigators. Cryo-EM data for the ABCG2-MZ29-Fab and ABCG2-MB136-Fab samples were collected at the electron microscopy facility at ETH Zurich (ScopeM); we thank P. Tittmann for technical support. Cryo-EM data for the ABCG2-MZ29 sample were collected at C-CINA, University of Basel; we thank K. Goldie, L. Kováčik and A. Fecteau-Lefebvre for technical support. We also thank J. Bloch for helpful discussions, F. Antoni, M. Scholler and D. Wifling (University of Regensburg) for technical assistance and helpful discussions and B. Sorrentino (St. Jude Children's Research Hospital) for providing the 5D3-producing hybridoma cell line.

Author contributions

I.M. expressed and purified ABCG2 and 5D3-Fab. I.M. and S.M.J. performed MST and thermostability experiments. S.M.J. reconstituted ABCG2 into liposomes and lipidic nanodiscs. J.K. prepared all cryo-grids and collected cryo-EM data for ABCG2-MZ29-Fab and ABCG2-MB136-Fab. I.M. and J.K. determined the structure of ABCG2-MZ29-Fab. J.K. determined the structure of ABCG2-MB136-Fab. N.M.I.T. and H.S. collected cryo-EM data and determined the structure of ABCG2-MZ29. I.M. and K.P.L. refined and validated the structures with the help of J.K. and N.M.I.T. M.Z. synthesized Ko143 and derivatives, and R.B. synthesized Fko143 and Fko132, under the supervision of K.-H.A. M.B. synthesized MB136. M.B., S.B., G.B., B.K. and A.B. designed MB136 and supervised and assisted in its synthesis. S.M.J. screened the compounds and performed all of the ATPase and transport assays. K.P.L., K.-H.A., S.M.J. and I.M. conceived the project. K.P.L., S.M.J. and I.M. planned the experiments. S.M.J., I.M. and K.P.L. wrote the manuscript; all authors contributed to revisions.

Competing interests

The authors declare no competing interests.

Additional information

Supplementary information is available for this paper at <https://doi.org/10.1038/s41594-018-0049-1>.

Reprints and permissions information is available at www.nature.com/reprints.

Correspondence and requests for materials should be addressed to K.-H.A. or K.P.L.

Publisher's note: Springer Nature remains neutral with regard to jurisdictional claims in published maps and institutional affiliations.

Methods

Expression and purification of human ABCG2. Human ABCG2, containing an amino (N)-terminal Flag tag, was expressed in HEK293-EBNA (Thermo Fisher Scientific) cells⁵² and purified as described previously²⁹. After transfection, the cells were solubilized with 1% *n*-dodecyl- β -D-maltopyranoside (DDM) and 0.1% cholesteryl hemisuccinate (CHS) (w/v) (Anatrace), ultracentrifuged at 100,000g, and the supernatant was then incubated with anti-Flag M2 affinity agarose gel (Sigma). ABCG2 was eluted with Flag peptide (Sigma), loaded into a Superdex 200 10/300 column (GE Healthcare) pre-equilibrated with 40 mM HEPES, pH 7.5, 150 mM NaCl, 0.026% DDM and 0.0026% CHS (w/v), and the peak fractions were collected.

Size-exclusion chromatography-based thermostability assay (SEC-TS).

Detergent-purified ABCG2 was incubated with or without 10 μ M of inhibitor (MZ29, MB136 or FKo143) or 50 μ M of transport substrate (E_i S) for 10 min at room temperature. 100 μ l samples were aliquoted into thin-walled PCR tubes and heated at one temperature, ranging from 30–75 °C, for 10 min in a Bio-Rad Thermocycler. The samples were cooled on ice immediately, spun at 100,000g for 20 min at 4 °C and then loaded onto a TSKgel G3000SWXL column (Tosoh Bioscience). Curves were plotted using the sigmoidal dose-response (variable slope) tool in GraphPad Prism 7 (GraphPad Software).

Expression and purification of 5D3-Fab. 5D3 hybridoma cells, producing the 5D3 monoclonal antibody, were obtained from B. Sorrentino³⁶. The cells were cultured in WHEATON CELLLine Bioreactors, according to the manufacturer's protocol, and 5D3-Fab was then purified from the supernatant, as described in the Fab Preparation Kit protocol (Thermo Fisher Scientific).

ABCG2-nanodisc preparation. Membrane scaffold protein (MSP) 1D1 was expressed and purified as described previously⁵³. Brain polar lipid (BPL)/CHS (4:1) (w/w) was solubilized with a 3 \times molar excess of sodium cholate using an ultrasonic bath. Solubilized BPL/CHS (4:1) (w/w) was mixed with MSP 1D1 and detergent-purified ABCG2 at a molar ratio of 100:5:0.2 (lipid/MSP/ABCG2). BioBeads were added, and the sample was incubated at 4 °C overnight. BioBeads were removed, and the sample was spun at 100,000g before being loaded into a Superdex 200 10/300 column (GE Healthcare) pre-equilibrated with 25 mM HEPES, pH 7.5, and 150 mM NaCl and used for ATPase assays. For cryo-EM studies in the presence of Fab, the sample was prepared as described above except ABCG2 was first mixed with a three-fold molar excess of Fab and then 10 μ M inhibitor (MZ29 or MB136) before reconstitution into nanodiscs. For cryo-EM studies in the absence of Fab, the sample was mixed with 10 μ M MZ29 before reconstitution.

ABCG2-liposome preparation. A BPL/cholesterol (BPL/chol) (Avanti Polar Lipids) mixture was prepared at a 4:1 (w/w) ratio as described previously⁵⁴. Briefly, the BPL/chol mixture was extruded through a 400-nm polycarbonate filter and destabilized with 0.17% (v/v) Triton X100. Detergent-purified ABCG2 was then mixed with BPL/chol at a 100:1 (w/w) lipid/protein ratio. Detergent was removed with BioBeads, and proteoliposomes were spun at 100,000g, resuspended in 25 mM HEPES, pH 7.5, 150 mM NaCl at a final lipid concentration of 10 mg ml⁻¹, and the reconstitution efficiency was determined⁵⁵.

Transport assays. ABCG2 proteoliposomes were extruded through a 400-nm polycarbonate filter and diluted to 4 mg ml⁻¹ lipid in 25 mM HEPES, pH 7.5, 150 mM NaCl, 5 mM MgCl₂ and 50 μ M [³H]E₁S was added, in the absence or presence of 0.5 μ M of unlabeled competitor (with the exception of MB136* and tariquidar* in Fig. 4b, where 10 μ M was used), and incubated for 5 min at 30 °C. The transport reaction was initiated by the addition of 2 mM ATP. To stop the reaction, samples were removed, added to ice-cold stop buffer (25 mM HEPES, pH 7.5, 150 mM NaCl, 100 μ M unlabeled E₁S) and filtered using a Multiscreen vacuum manifold (MSFBN6B filter plate, Millipore). Radioactivity trapped on the filters was measured using a Perkin Elmer 2450 Microbeta2 microplate scintillation counter. Curves were plotted using the nonlinear regression Michaelis–Menten analysis tool and initial transport rates from 30 s to 2 min were determined using linear regression in GraphPad Prism 7. Rates were corrected for the orientation of ABCG2 in proteoliposomes as determined and described in ref. ²⁹. The normalized initial transport rates, with the uninhibited rates set to 100%, were then plotted.

ATPase assays. ATP hydrolysis activity was measured using a technique described previously⁵⁶. All reactions were performed at 37 °C in the presence of 2 mM ATP and 10 mM MgCl₂. For ATPase assays in proteoliposomes, experiments were completed with 50 μ M E₁S in the presence or absence of 0.5 μ M competitor. For assays in ABCG2 nanodiscs, the molar ratios of Ko143 or MB136 were varied in relation to ABCG2 to determine the functional stoichiometry for both compounds. ATPase rates were determined using linear regression in GraphPad Prism 7. Rates were corrected for the orientation of ABCG2 in proteoliposomes as determined and described in ref. ²⁹. The normalized ATPase rates, with the uninhibited rates set to 100%, were then plotted.

Microscale thermophoresis binding assay (MST). The binding of FKo143 (G2 + FKo143) or FKo132 (G2 + FKo132) to ABCG2 or ABCG2–Fab was

measured using microscale thermophoresis with a NanoTemper monolith NT.115 instrument⁵⁷. A range of concentrations of detergent-purified ABCG2 (0.11 nM–3.65 μ M) were incubated with 50 nM of FKo143 or FKo132 for 10 min in assay buffer (40 mM HEPES, pH 7.5, 150 mM NaCl, 0.026% DDM and 0.0026% CHS). To check the effect of 5D3-Fab on the binding of FKo143 to ABCG2, two separate samples were measured. In the first sample, ABCG2 was first preincubated with a 2.5 \times molar excess of 5D3-Fab for 10 min prior to the addition of FKo143 (G2 + Fab + FKo143). In the second sample, ABCG2 was first preincubated with FKo143 for 10 min prior to the addition of 5D3-Fab (G2 + FKo143 + Fab). The samples were then loaded into NanoTemper standard glass capillaries, and microthermophoresis was carried out using 60% LED power and 40% MST. K_D values were calculated using the mass action equation via the NanoTemper software.

Sample preparation and cryo-EM data acquisition. The cryo grids were prepared using a Vitrobot Mark IV (FEI) with the environmental chamber set at 100% humidity and 4 °C. An aliquot of 4 μ l purified ABCG2–MZ29–Fab, ABCG2–MB136–Fab or ABCG2–MZ29, at a protein concentration of approximately 0.4 mg ml⁻¹, was applied to glow-discharged Quantifoil (1.2/1.3) 300 mesh Cu grids. After being blotted with filter paper for 2.0 s, the grids were flash frozen in a mixture of propane and ethane, then cooled with liquid nitrogen.

The final datasets were composed of 4,094, 2,468 and 9,244 micrographs for the ABCG2–MZ29–Fab, ABCG2–MB136–Fab and ABCG2–MZ29 samples, respectively. Movies were recorded semiautomatically with SerialEM on a Titan Krios operated at 300 keV and equipped with a Gatan K2 Summit and a GIF Quantum LS energy filter. Images were recorded in super-resolution counting mode with a defocus range of –0.5 to –2.5 μ m.

Super-resolution pixel sizes were 0.42 Å/pixel, 0.5325 Å/pixel and 0.4058 Å/pixel for the ABCG2–MZ29–Fab, ABCG2–MB136–Fab and ABCG2–MZ29 movies, respectively. For the ABCG2–MZ29–Fab sample, each stack was exposed for 10 s with an exposure time of 0.2 s per frame, resulting in 50 frames per stack and a frame dose of 2.0 e⁻/Å². For ABCG2–MZ29, the data collection parameters were the same as for ABCG2–MZ29–Fab, but with the first frame removed. For the ABCG2–MB136–Fab sample, 15-s stacks, with 0.25-s frames and a frame dose of 1.55 e⁻/Å², were recorded. All stacks were gain normalized, motion corrected, dose weighted and then binned two-fold with MotionCor2 (ref. ⁵⁸). The defocus values were estimated on the non-dose-weighted micrographs with Gctf⁵⁹.

Image processing. From the ABCG2–MZ29–Fab micrographs a total of 587,743 particles were picked with Gautomatch (<http://www.mrc-lmb.cam.ac.uk/kzhang/>). Image processing was performed in RELION 2.0 (ref. ⁶⁰). The picked particles were screened by five rounds of 2D classification. Almost all particles (543,842) were correctly assigned to 2D classes, selected and finally subjected to a global angular search 3D classification with five classes. A total of 284,831 particles were combined from the good 3D classes. These particles were applied for initial autorefinement with a soft mask resulting in a 3D reconstruction with an overall resolution of 3.19 Å (for map with applied C2 symmetry) and 3.25 Å (non-symmetrized map). After regrouping of the particles and adapting the soft mask in the following 3D refinement, the map resolution improved to 3.1 Å.

Image processing of the ABCG2–MB136–Fab particles was performed both in RELION 2.0 (ref. ⁶⁰) and CryoSPARC⁶¹. A total of 529,097 ABCG2–MB136 particles were picked with Gautomatch and 2D classified in RELION 2.0. After five rounds of 2D classification and selection, we obtained a final dataset of 424,235 particles. These particles were used for 3D classification with three classes. From two good 3D classes, 306,913 particles were selected for the first 3D autorefinement with C1 and C2 symmetry. After post-processing, maps with resolutions of 3.65 Å and 3.50 Å were obtained, respectively. In parallel, the same set of particles was processed in CryoSPARC. Ab initio 3D reconstruction followed by homogenous 3D refinement (symmetry C1) and map sharpening resulted in map at 3.60-Å resolution. The CryoSPARC map showed much better asymmetric density inside the ABCG2 molecule, corresponding to MB136, than the map from RELION 2.0.

For ABCG2–MZ29, data were processed using RELION 2.1b. Particles (2,098,186) were picked automatically by Gautomatch, binned 4 \times and 2D classified in RELION. After three rounds of 2D classification, the remaining 1,087,316 particles were subjected to 3D classification into ten classes (applying C2 symmetry). The particles from the best three classes (549,517 in total) were extracted again, this time unbinned, and subjected to 3D classification into five classes (using C2 symmetry). Four classes corresponded to “good” classes, and three of these classes were very similar to each other. Particles in those three classes (402,348 in total) were combined to give a final reconstruction, applying C2 symmetry, with the RELION autorefinement procedure. After automated masking and post-processing, the resolution was estimated to be 3.56 Å.

All ABCG2–MZ29–Fab, ABCG2–MB136–Fab and ABCG2–MZ29 maps were post-processed, including soft masking, and using the automatically determined B-factor sharpening routines. The resolutions were estimated with the gold-standard Fourier shell correlation (FSC) 0.143 cutoff criterion⁶². ResMap⁶³ was used to calculate the local resolution maps. In the case of ABCG2–MZ29, maps filtered by local resolution were also created in RELION.

Model building and refinement. For model building, we used the post-processed map of ABCG2–MZ29–Fab at an overall resolution of 3.1 Å. The quality of the EM density was of excellent quality and allowed the de novo building of ABCG2 and the variable domain of 5D3–Fab. The Coot program⁶⁴ was used for all model building steps and the previous ABCG2–5D3(Fab) model (PDB 5NJ3 and PDB 5NIV) was docked into the EM density and used as an initial reference²⁹. The MZ29 coordinates and restraints were generated using eLBOW⁶⁵ and fitted into the EM density using Coot. The complete ABCG2–MZ29–Fab atomic model was refined against the working map in Phenix⁶⁶ using the program phenix.real_space_refine at a resolution limit of 3.1 Å. For the final round of model refinement, we performed global real-space refinement with standard geometry restraints as well as rotamer, Ramachandran plot, C β , noncrystallographic symmetry (NCS) and secondary structure restraints, coupled to reciprocal-space refinement of the *B* factors. The quality of the final model was analyzed using MolProbity⁶⁷, and the refinement statistics are in Table 1. For validation of the refinement, random shifts (mean value of 0.3 Å) were introduced into the coordinates of the final refined model using the program phenix.pdbtools⁶⁶, then refinement was done with phenix.real_space_refine (using the same parameters as described previously) against the first unfiltered half-map (half-map 1). The overlay between the FSC curve of the model with random displacements refined against half-map 1 versus half-map 1 and the FSC curve of the same model versus half-map 2 (against which it was not refined) indicated that no over-refinement took place.

For the ABCG2–MZ29 structure, we used the ABCG2–MZ29 subcomplex structure, obtained from the ABCG2–MZ29–Fab sample, as a starting model for rebuilding into the post-processed and RELION local-resolution filtered maps. The structure was very similar with the exception of EL3, which needed rebuilding. After manual rebuilding in Coot, the structure was refined and validated similarly to the ABCG2–MZ29–Fab structure.

For the ABCG2–MB136–Fab structure, we docked the refined ABCG2–Fab subcomplex structure, obtained from the ABCG2–MZ29–Fab sample, into the EM density using Coot. The MB136 coordinates and restraints were generated using eLBOW and fitted into the EM density using Coot.

Figure preparation. Figures were prepared using the programs PyMOL (The PyMOL Molecular Graphics System, DeLano Scientific, <http://www.pymol.org/>) and GraphPad Prism 7 (GraphPad Software).

Life Sciences Reporting Summary. Further information on experimental design is available in the Life Sciences Reporting Summary.

Data availability. Atomic coordinates were deposited in the Protein Data Bank under accession codes PDB 6ETI (ABCG2–MZ29–Fab, 5D3–Fab variable domain only), PDB 6FFC (ABCG2–MZ29) and PDB 6FEQ (ABCG2–MB136–Fab; 5D3–Fab variable domain only). EM data for the three structures were deposited in the Electron Microscopy Data Bank under accession codes EMD-3953 (ABCG2–MZ29–Fab), EMD-4256 (ABCG2–MZ29) and EMD-4246 (ABCG2–MB136–Fab). Source data for Figs. 1a–c, 4b and 6a and Supplementary Fig. 1b are available in Supplementary Dataset 1. All other data are available from the corresponding authors upon reasonable request.

References

- Geisse, S., Jordan, M. & Wurm, F. M. Large-scale transient expression of therapeutic proteins in mammalian cells. *Methods Mol. Biol.* **308**, 87–98 (2005).
- Ritchie, T. K. et al. Chapter 11 - Reconstitution of membrane proteins in phospholipid bilayer nanodiscs. *Methods Enzymol.* **464**, 211–231 (2009).
- Geertsma, E. R., Nik Mahmood, N. A., Schuurman-Wolters, G. K. & Poolman, B. Membrane reconstitution of ABC transporters and assays of translocator function. *Nat. Protoc.* **3**, 256–266 (2008).
- Schaffner, W. & Weissmann, C. A rapid, sensitive, and specific method for the determination of protein in dilute solution. *Anal. Biochem.* **56**, 502–514 (1973).
- Chifflet, S., Torriglia, A., Chiesa, R. & Tolosa, S. A method for the determination of inorganic phosphate in the presence of labile organic phosphate and high concentrations of protein: application to lens ATPases. *Anal. Biochem.* **168**, 1–4 (1988).
- Wienken, C. J., Baaske, P., Rothbauer, U., Braun, D. & Duhr, S. Protein-binding assays in biological liquids using microscale thermophoresis. *Nat. Commun.* **1**, 100 (2010).
- Zheng, S. Q. et al. MotionCor2: anisotropic correction of beam-induced motion for improved cryo-electron microscopy. *Nat. Methods* **14**, 331–332 (2017).
- Zhang, K. Gctf: Real-time CTF determination and correction. *J. Struct. Biol.* **193**, 1–12 (2016).
- Kimanius, D., Forsberg, B. O., Scheres, S. H. & Lindahl, E. Accelerated cryo-EM structure determination with parallelisation using GPUs in RELION-2. *eLife* **5**, e18722 (2016).
- Punjani, A., Rubinstein, J. L., Fleet, D. J. & Brubaker, M. A. cryoSPARC: algorithms for rapid unsupervised cryo-EM structure determination. *Nat. Methods* **14**, 290–296 (2017).
- Rosenthal, P. B. & Henderson, R. Optimal determination of particle orientation, absolute hand, and contrast loss in single-particle electron cryomicroscopy. *J. Mol. Biol.* **333**, 721–745 (2003).
- Kucukelbir, A., Sigworth, F. J. & Tagare, H. D. Quantifying the local resolution of cryo-EM density maps. *Nat. Methods* **11**, 63–65 (2014).
- Emsley, P., Lohkamp, B., Scott, W. G. & Cowtan, K. Features and development of Coot. *Acta Crystallogr. D Biol. Crystallogr.* **66**, 486–501 (2010).
- Moriarty, N. W., Grosse-Kunstleve, R. W. & Adams, P. D. electronic Ligand Builder and Optimization Workbench (eLBOW): a tool for ligand coordinate and restraint generation. *Acta Crystallogr. D Biol. Crystallogr.* **65**, 1074–1080 (2009).
- Adams, P. D. et al. PHENIX: a comprehensive Python-based system for macromolecular structure solution. *Acta Crystallogr. D Biol. Crystallogr.* **66**, 213–221 (2010).
- Chen, V. B. et al. MolProbity: all-atom structure validation for macromolecular crystallography. *Acta Crystallogr. D Biol. Crystallogr.* **66**, 12–21 (2010).

Life Sciences Reporting Summary

Nature Research wishes to improve the reproducibility of the work that we publish. This form is intended for publication with all accepted life science papers and provides structure for consistency and transparency in reporting. Every life science submission will use this form; some list items might not apply to an individual manuscript, but all fields must be completed for clarity.

For further information on the points included in this form, see [Reporting Life Sciences Research](#). For further information on Nature Research policies, including our [data availability policy](#), see [Authors & Referees](#) and the [Editorial Policy Checklist](#).

▶ Experimental design

1. Sample size

Describe how sample size was determined.

Figure 1a,b,c, Figure 4b, Figure 6a, Supplementary Figure 1b.

2. Data exclusions

Describe any data exclusions.

No data excluded

3. Replication

Describe whether the experimental findings were reliably reproduced.

All replicates were successful

4. Randomization

Describe how samples/organisms/participants were allocated into experimental groups.

Animals and humans were not used in the study, not applicable

5. Blinding

Describe whether the investigators were blinded to group allocation during data collection and/or analysis.

Animals and humans were not used in the study, blinding not applicable

Note: all studies involving animals and/or human research participants must disclose whether blinding and randomization were used.

6. Statistical parameters

For all figures and tables that use statistical methods, confirm that the following items are present in relevant figure legends (or in the Methods section if additional space is needed).

n/a Confirmed

- The exact sample size (n) for each experimental group/condition, given as a discrete number and unit of measurement (animals, litters, cultures, etc.)
- A description of how samples were collected, noting whether measurements were taken from distinct samples or whether the same sample was measured repeatedly
- A statement indicating how many times each experiment was replicated
- The statistical test(s) used and whether they are one- or two-sided (note: only common tests should be described solely by name; more complex techniques should be described in the Methods section)
- A description of any assumptions or corrections, such as an adjustment for multiple comparisons
- The test results (e.g. P values) given as exact values whenever possible and with confidence intervals noted
- A clear description of statistics including central tendency (e.g. median, mean) and variation (e.g. standard deviation, interquartile range)
- Clearly defined error bars

See the web collection on [statistics for biologists](#) for further resources and guidance.

► Software

Policy information about [availability of computer code](#)

7. Software

Describe the software used to analyze the data in this study.

GraphPad PRISM7, PyMOL, PHENIX, Coot, Relion 2.0, MotionCor2, Gctf, Gautomatch, Chimera, CryoSPARC.

For manuscripts utilizing custom algorithms or software that are central to the paper but not yet described in the published literature, software must be made available to editors and reviewers upon request. We strongly encourage code deposition in a community repository (e.g. GitHub). *Nature Methods* [guidance for providing algorithms and software for publication](#) provides further information on this topic.

► Materials and reagents

Policy information about [availability of materials](#)

8. Materials availability

Indicate whether there are restrictions on availability of unique materials or if these materials are only available for distribution by a for-profit company.

The synthetic compounds, apart from Ko143, Ko132, tariquidar and FTC, were synthesized exclusively for this project as described in the manuscript.

9. Antibodies

Describe the antibodies used and how they were validated for use in the system under study (i.e. assay and species).

5D3 antibody (reference 36 in the manuscript).

10. Eukaryotic cell lines

a. State the source of each eukaryotic cell line used.

HEK293 EBNA (Thermo Fisher Scientific).

b. Describe the method of cell line authentication used.

No

c. Report whether the cell lines were tested for mycoplasma contamination.

No

d. If any of the cell lines used are listed in the database of commonly misidentified cell lines maintained by [ICLAC](#), provide a scientific rationale for their use.

N/A

► Animals and human research participants

Policy information about [studies involving animals](#); when reporting animal research, follow the [ARRIVE guidelines](#)

11. Description of research animals

Provide details on animals and/or animal-derived materials used in the study.

N/A

Policy information about [studies involving human research participants](#)

12. Description of human research participants

Describe the covariate-relevant population characteristics of the human research participants.

N/A